UNIVERSITY OF BIRMINGHAM
University of Birmingham Research at Birmingham

Numerical and experimental study on the aerodynamic force coefficients of railway vehicles on an embankment in crosswind

Noguchi, Yuhei; Suzuki, Minoru; Baker, Chris; Nakade, Koji

DOI:
10.1016/j.jweia.2018.11.019

License:
Creative Commons: Attribution-NonCommercial-NoDerivs (CC BY-NC-ND)

Document Version
Peer reviewed version

Citation for published version (Harvard):
Noguchi, Y, Suzuki, M, Baker, C & Nakade, K 2019, 'Numerical and experimental study on the aerodynamic force coefficients of railway vehicles on an embankment in crosswind', *Journal of Wind Engineering and Industrial Aerodynamics*, vol. 184, pp. 90-105. https://doi.org/10.1016/j.jweia.2018.11.019

Link to publication on Research at Birmingham portal

Publisher Rights Statement:
Checked for eligibility 06/12/2018

https://doi.org/10.1016/j.jweia.2018.11.019

General rights
Unless a licence is specified above, all rights (including copyright and moral rights) in this document are retained by the authors and/or the copyright holders. The express permission of the copyright holder must be obtained for any use of this material other than for purposes permitted by law.

•Users may freely distribute the URL that is used to identify this publication.
•Users may download and/or print one copy of the publication from the University of Birmingham research portal for the purpose of private study or non-commercial research.
•User may use extracts from the document in line with the concept of 'fair dealing' under the Copyright, Designs and Patents Act 1988 (?)
•Users may not further distribute the material nor use it for the purposes of commercial gain.

Where a licence is displayed above, please note the terms and conditions of the licence govern your use of this document.

When citing, please reference the published version.

Take down policy
While the University of Birmingham exercises care and attention in making items available there are rare occasions when an item has been uploaded in error or has been deemed to be commercially or otherwise sensitive.

If you believe that this is the case for this document, please contact UBIRA@lists.bham.ac.uk providing details and we will remove access to the work immediately and investigate.

Download date: 05. May. 2023

Numerical and experimental study on the aerodynamic force coefficients of railway vehicles on an embankment in crosswind

Yuhei Noguchi[a,*], Minoru Suzuki[a], Chris Baker[b], Koji Nakade[a]

[a]Railway Technical Research Institute
[b]Birmingham Centre for Railway Research and Education

Keywords: wind tunnel tests, embankment scenario, CFD simulation, LES and Train aerodynamics

ABSTRACT

It is necessary to obtain the aerodynamic force coefficients of the train on the embankment for the assessment of the running safety in a crosswind. In general, wind tunnel tests are conducted using the static train model on the embankment model. In this paper, the influence of the airflow condition and the distance from the upstream end of the embankment model to the train model on the aerodynamic force coefficients is investigated. In the wind tunnel tests, the side force coefficients (C_S) reached their maximum values at a yaw angle of 50° in smooth flow while they reached their maximum values at a yaw angle of 90° in atmospheric boundary layer (ABL) flow. Large-eddy simulation (LES) was made on the flow around the train model on the embankment, and it was found that C_S became larger as the upstream embankment length became smaller owing to the vortex generated near the upstream end of the embankment at the yaw angle of 50°. LES on the flow around the embankment model showed that the distance over which the flow field was affected by this vortex was 16 times the height of the embankment model in smooth flow, and it was 12 times in ABL flow at the yaw angle of 50°.

1. Introduction

To evaluate the running safety of railway vehicles running under a strong crosswind, it is necessary to estimate the aerodynamic forces acting on trains that are caused by the crosswind, as well as understand the flow field around the trains. Many research studies have been carried out to investigate the influence of the crosswind on trains (Baker, 1991; Baker et al., 2009; Sanquer et al., 2004; Khier et al., 2000; Hemida and Krajnović, 2010; Baker, 2013). In addition, the international standard for the international interoperability of the railway vehicles has been set (EN 14067-6, 2010). Based on the standard, it is required to run wind tunnel tests or computational fluid dynamics (CFD) analyses to determine the aerodynamic force coefficients of trains running under the crosswind in order to evaluate the trains' running safety.

A train travels on raised ground for the embankment scenario when compared to the flat ground scenario. Therefore, the train on the embankment is exposed to a stronger wind than that on the flat ground, which can increase the aerodynamic force acting on the train. Hence, embankments are considered high-risk scenarios. Various research studies on railway vehicles running on embankments have been conducted (Baker, 1986; Suzuki et al., 2003; Bocciolone et al., 2008; Cheli et al., 2010; Schober et al., 2010; Diedrichs et al., 2007; Tomasini et al., 2014). It is normal in wind tunnel tests to measure the aerodynamic forces acting on the train model statically set on the embankment model, which is installed in an airflow with a wind direction similar to the train model. However, this method has two major defects. First, the relative movement between trains and embankments is not correctly

reproduced. Hence, experiments using the moving train models and the CFD analyses have been conducted to investigate the effect of the relative movement between the train model and the ground on aerodynamic force coefficients (Baker, 1986; Bocciolone et al., 2008; Dorigatti et al., 2015; Suzuki, 2016; Krajnović et al., 2012; Nakade, 2014; Premoli et al., 2016). Second, the end layouts of the embankment models can affect the flow field around a train model when using static train model. Schober et al. (2010) and Diedrichs et al. (2007) indicated that the finite-length embankment model, which does not reach the side walls of the wind tunnel, generates an unrealistic flow on the leeward side of the embankment model subjected to the yawed wind. Diedrichs et al. (2007) performed experiments and CFD analyses to extend the embankment model to the side walls of the wind tunnel at the yaw angle of 30°. In addition, Tomasini et al. (2014) investigated the influence of the end layouts and the length of the embankment model on the aerodynamic force coefficients using wind tunnel tests. Tomasini et al. (2014) referred to the test condition in which the embankment model is extended to the side walls of the wind tunnel as a pseudo-infinite embankment configuration, and regarded this condition as the flow field closest to the actual flow around the real embankment. Tomasini et al. (2014) indicated that the distance from the upstream end of the embankment model to the train model is a key parameter for determining aerodynamic force coefficients at yaw angles of 40° and 50°.

In Europe, the running safety under a crosswind is mainly concerned with high-speed trains with maximum running speeds of over 250 km/h. In this case, the yaw angle relative to the train is less than 30° even if the crosswind blows in a direction perpendicular to the rail. Thus, attention is drawn to the condition under which the yaw angle relative to the train is small. On the other hand, in Japan, the railway that is subjected to strong wind is the meter gauge railway, which has a maximum speed of 130 km/h. In fact, all the wind-induced accidents in Japan have taken place on the meter gauge railway, while no wind-induced accident has occurred on the high-speed railway that has a standard gauge. The maximum running speed is about 110 km/h in most of the Japanese meter gauge railways; consequently, the yaw angle relative to the train is more than 30° in contrast to the case of the high-speed trains with a crosswind blowing in the direction perpendicular to the rail. It is known that the ground scenarios have a great influence on the aerodynamic force coefficients in the case of large yaw angles (Bocciolone et al., 2008 and Cheli et al., 2010). In Japan, wind tunnel tests were carried out to obtain the aerodynamic force coefficients for various combinations of trains and ground scenarios, such as bridges, viaducts, and embankments (Suzuki et al., 2003 and Suzuki et al., 2014).

As mentioned above, the velocity of the wind relative to the train running under the crosswinds is a resultant of the velocity of the natural wind and that of the train (Fig. 1). Consequently, the still train in operation is hit by a wind that has a turbulence with the vertical profile of speed. As the train travels faster, the wind relative to the train has a more uniform profile with less turbulence (Baker, 2010). Previous work on the effect of turbulence on the aerodynamic characteristics of trains investigated the time-averaged aerodynamic forces and aerodynamic admittance functions (Bocciolone et al., 2008; Robinson and Baker, 1990; Cheli et al., 2013; Suzuki and Hibino, 2016; García et al., 2015). However, to the best of the authors' knowledge, there is limited research on the effect of the airflow conditions on the trains located on the embankment, which is one of the most typical railway scenarios. In addition, it is unclear why the distance from the upstream end of the embankment model to the train model is the key parameter for determining aerodynamic force coefficients at yaw angles of 40° and 50° (Tomasini et al., 2014).

The goals of this study are to determine why the distance from the upstream end of the embankment model to the train model affects the aerodynamic force coefficients at a yaw angle of 50°, and to understand the effect of the airflow condition on the aerodynamic characteristics of the train model on the embankment model. Thus, in this study, wind tunnel tests were carried out to obtain aerodynamic force coefficients of 1:40 scale train models statically mounted on

8-m high embankment of the same scale. The models were tested in both atmospheric boundary layer (ABL) flow and smooth flow. The aerodynamic force coefficients obtained in each airflow were compared. In addition, large-eddy simulation (LES) was conducted to reproduce the wind tunnel experiments and visualize the flow field around the train model on the embankment model at yaw angles of 90° and 50° in smooth flow. In LES analyses, the distance from the end of the embankment model to the train model was varied at a yaw angle of 50°, and its effect on the aerodynamic force acting on the train model was investigated. Finally, LES on the flow around the embankment model was conducted in both ABL flow and smooth flow. The influence of the airflow condition on the flow field around the embankment model was investigated. The relation between the flow field around the embankment model and the aerodynamic force acting on the train model was also examined.

This paper is organized as follows. The set-up of the wind tunnel tests is described in Section 2. The numerical method of LES, the geometry of the models, and the computational domains, as well as the boundary conditions are described in Section 3. The aerodynamic force coefficients obtained in the wind tunnel tests are presented in Section 4.1. The results of the LES on the flow around the train models on the embankment model are described in Section 4.2, and those on the flow around the embankment model without train models are described in Section 4.3. Section 5 presents the conclusions.

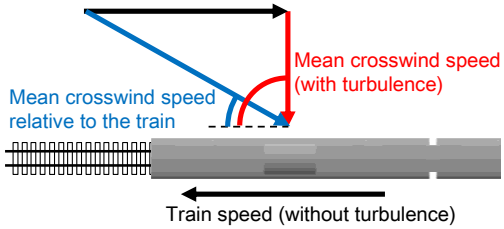

Fig. 1 Wind speed and yaw angle relative to the train

2. Experimental set-up of wind tunnel tests

Wind tunnel tests were carried out in the closed test section of a large-scale low-noise wind tunnel owned by the Railway Technical Research Institute in Japan. The test section is 5 m wide, 3 m high, and 20 m long. The models were statically set on the turntable, which was located 16.8 m leeward from the entrance of the test section. The model of the embankment shown in Fig. 2 has the same layout as that used by Suzuki et al., 2003. The scale of the model was 1:40. The height of the embankment model (h_{emb}) was 8 m (200 mm on the reduced scale). The single-track ballast and rail were placed on top of the embankment. The height of the rail level was 8.72 m from the floor (218 mm on the reduced scale). The slope gradient of the embankment was 1:1.5. The cross sections of the train models are shown in Fig. 3. The shape of the train roof has a significant influence on the aerodynamic forces acting on the train under a crosswind (Suzuki et al., 2003). Thus, the aerodynamic forces acting on five types of train models with various roof curvatures were measured. The tested roof curvatures were 1840 mm for train A and train B; 5000 mm for train C; 8000 mm for train D; and infinity for train E, which meant that the roof had no curvature. All of the train models were leading vehicles of the meter-gauge railway in Japan, and all models had bluff noses, not streamlined noses. The shapes of the leading vehicle models were identical to the actual leading vehicles, including the underfloor equipment. However, neither pantographs nor coupling parts were replicated in the train models for the experiments. The lower parts of wheels were cut to avoid contact with the rail. The specifications of the train models are listed in Table 1.

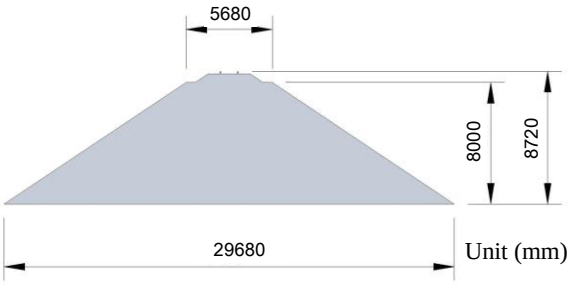

Fig. 2 Layout of the embankment model

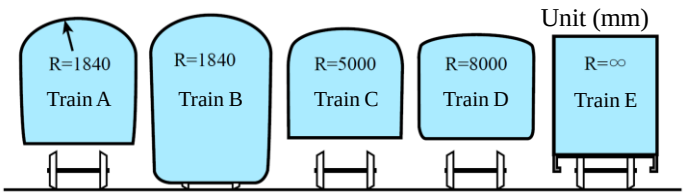

Fig. 3 Cross sections of the train models

Table 1 Specifications of the train models

Unit (m)	Train A	Train B	Train C	Train D	Train E
Length of the car body	20.8	21.2	19.5	20.0	18.9
Height of the car body	3.08	3.88	2.64	2.48	2.88
Rail level ~ center of the car body	2.56	2.16	2.36	2.24	2.32
Radius of the roof	1.84	1.84	5.00	8.00	Infinity

The tests were conducted under both smooth flow and ABL flow conditions. The vertical profiles of the mean streamwise wind speed U/U_0 and the streamwise turbulence intensity I_u at the center of the turntable without installment of any experimental models are shown in Fig. 4. The wind speed U_0 is the mean wind velocity measured by a pitot tube installed 5 m upstream from the center of the turntable and 1.8 m high from the floor. In the smooth flow case, the boundary layer develops inevitably on the floor. The boundary layer thickness $\delta_{99\%}$ in the smooth flow case was 180 mm on the reduced scale ($\delta_{99\%}/h_{emb}$ = 0.9), and the turbulence intensity I_u was 0.3% on the outside of the boundary layer. The boundary layer thickness is relatively large compared to the embankment height. Therefore, the side force coefficients in the smooth flow case are likely to be underestimated when compared with an ideal block-profile case. The ABL flow was generated by the barrier, the spires, and the roughness blocks located on the floor on the windward side of the models. The power law exponent of the wind profile of ABL flow was 0.26. The longitudinal integral length scale L_u^x was approximately 800 mm on the reduced scale, which was 1.6 times as long as the length of the car body.

The aerodynamic forces acting on the train models were measured by the six-component sting balance (NISSHO, LMC-6522-38/Z80) installed in the train models. The balance was fixed in the dummy vehicle model next to the leading vehicle model, and the leading vehicle model was supported by the sting balance. The sampling frequency was 100 Hz, and the cut-off frequency of the low-pass filter was 30 Hz. The period of the data acquisition was 30 s in the smooth flow case, while it was 45 s in the ABL flow case. The three-component aerodynamic force coefficients, which have a great influence on the overturn of trains, are defined as follows:

$$C_S = S/(1/2\rho U_{ref}^2 A_{ref}) \qquad C_L = L/(1/2\rho U_{ref}^2 A_{ref}) \qquad C_M = M/(1/2\rho U_{ref}^2 A_{ref} h_{ref}) \quad (1)$$

where S is the time-averaged side force; L is the time-averaged lift force; M is the time-averaged rolling moment around the center of the track on the rail level; ρ is the density of the air; U_{ref} is the reference velocity; h_{ref} is a reference length of 3 m (full scale); and A_{ref} is a reference area of 10 m^2 (full scale). In the smooth flow case, U_{ref} is equal to the velocity U_0, which is measured by the pitot tube installed 5 m upstream from the center of the turntable and 1.8 m high from the floor. In the ABL flow case, U_{ref} is the velocity at 0.318 m height (reduced scale) above the floor at the center

of the turntable without installment of any experimental models. This position corresponds to 4m height (full scale) above the rail level on the embankment, and it is nearly the same height as the top of the train. In this case, U_0 is converted to U_{ref} using the wind velocity profile shown in Fig. 4, that is, U_{ref} is equal to $0.63U_0$ in the ABL flow case. The reference system of the aerodynamic forces is shown in Fig. 5. It is fixed to the car body and its origin is coincident with the center of the track on the rail level. In the ABL flow case, the flow velocity in the streamwise and the vertical direction above the embankment model without train models was measured by a hot-wire anemometer with X wire probe (DANTEC 55P63). The experimental conditions of the velocity measurement are described in Saitou et al. (2008). However, the results presented in this report were obtained using the new jigs of the anemometer, which are improved from those used in Saitou et al. (2008).

The tests were conducted at four yaw angles (β = 30°, 50°, 70°, and 90°). The photographs of the tests are shown in Fig. 6. The embankment model was extended to the side walls of the wind tunnel except the leeward side of the embankment that was set at the yaw angle of 30°. In addition, the dummy vehicle models on the rear side of the leading vehicle were extended to the side wall as well as the embankment model. The distance from the front of the leading vehicle model to the end of the embankment model on the upstream side is 190 m on the full scale at the yaw angle of 30°, which is regarded as the pseudo-infinite embankment configuration referred to by Tomasini et al. (2014). The wind velocity U_0 was set at 20 m/s, 25 m/s, and 30 m/s. The maximum Reynolds numbers based on the height of the car body and U_{ref} were approximately 1.5×10^5 and 0.9×10^5 in the smooth flow case and the ABL case, respectively, which were similar values to those shown in Tomasini et al. (2014). The blockage ratio was 9%. The blockage correction was not applied in this study.

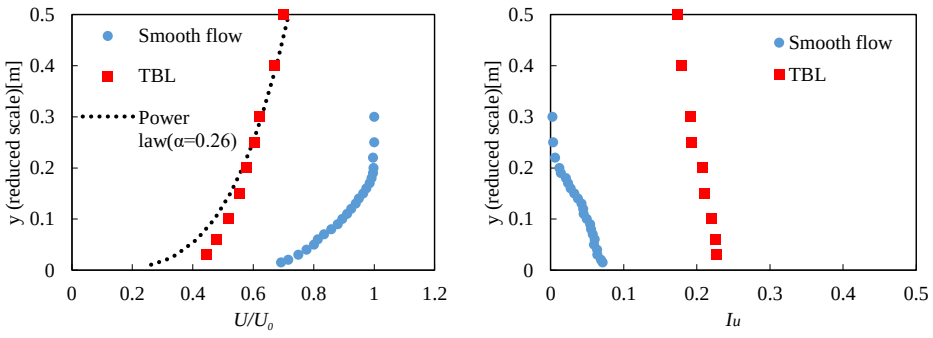

Fig. 4 Vertical profiles of the mean streamwise wind speed and streamwise turbulence intensity

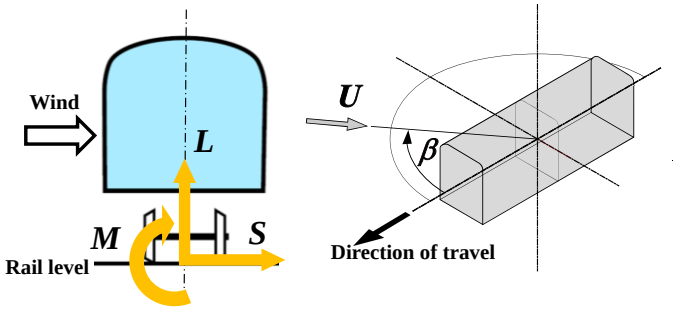

Fig. 5 Reference system of the aerodynamic forces

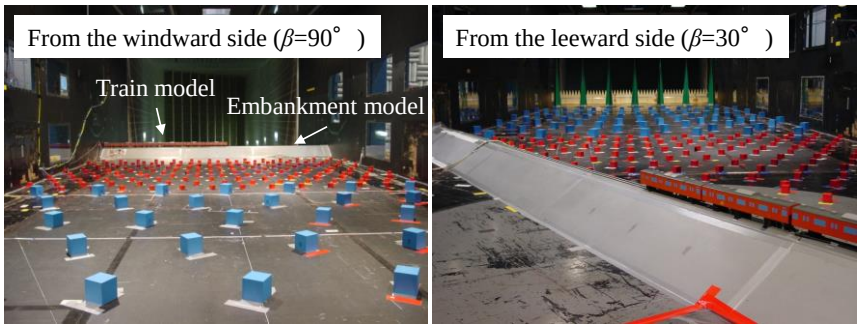

Fig. 6 Wind tunnel tests

3. Large-eddy simulation

3.1 Flow around train models on an embankment model

To reproduce the wind tunnel tests in smooth flow, LES was carried out using the train model whose shape was almost the same as that used in the tests at yaw angles of 90° and 50°. In addition, the distance from the side wall of the wind tunnel to the train model was varied in LES using the simple geometry train model at the yaw angle of 50°, and the relation between the distance and the aerodynamic forces on the train model was investigated.

3.1.1 Model description

The train C model and the simplified train model are used in the LES analyses. The geometries of the train models are shown in Fig. 7. The geometry of the train C model used in LES is identical to that in the experiments except for the rooftop and underfloor equipment details. To create the simplified train model, the bogies, rooftop, and underfloor equipment are removed from the train C model. The geometry of the embankment model is the same as that in the experiments. The embankment model and the dummy vehicle model are extended to the side walls of the computational domain in the same way as in the experiments. The dummy vehicle model has the same cross section as the leading vehicle model and does not have any underfloor or rooftop equipment. The height and the longitudinal length of the car body of the train model are h = 2.64/40 = 0.066 m and l = 19.5/40 = 0.488 m = 7.39h. The height of the embankment is h_{emb} = 8/40 = 0.2 m = 3.03h. The smooth flow cases at yaw angles of 90° and 50° were analyzed. For the train C model, the leading vehicle model is located in the middle of the computational domain as in the experiments. For the simplified train model, the leading vehicle model is located at positions $8h_{emb}$ and $4h_{emb}$ from the middle of the computation domain in the longitudinal direction of the embankment in order to investigate the influence of the distance from the side wall of the computational domain to the train model.

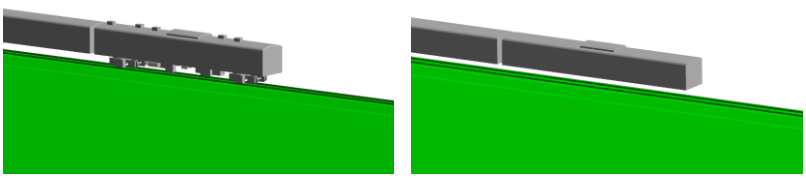

Fig. 7 Train C model and simplified train model

3.1.2 Numerical method

Numerical analyses were conducted using the commercial CFD code "Advance/ FrontFlow/ red ver. 5.2," which has been successfully used to analyze the flow around automobiles (Tsubokura et al., 2009). This code was originally developed for the "Frontier Simulation Software for Industrial Science" project in Japan. The governing equations are the spatially filtered continuity and Navier–Stokes equations for an incompressible flow. The standard Smagorinsky model is used to model the sub-grid scale stresses. The value of the Smagorinsky coefficient is set as 0.1. In the vicinity of the wall, Van–Driest-type damping function is adopted to reduce the sub-grid scale eddy viscosity near the wall. The governing equations are discretized by the vertex-centered unstructured finite volume method. The second-order central differencing scheme is applied for the spatial derivatives, and a blend of the 95% second-order central differencing scheme and the 5% first-order upwind scheme for the convection term is used for numerical stability. The time integration is done using the Crank–Nicolson second-order scheme. The SIMPLEC algorithm is used for the pressure–velocity coupling. The details of this code can be found in Tsubokura et al. (2009).

3.1.3 Computational domain and boundary condition

The computational domain is shown in Fig. 8. The computational domain has a height of 3 m (= 45.5h = 15h_{emb}) and a width of 5 m (= 75.8h = 25h_{emb}), and has dimensions similar to those of the test section of the experiments. In the streamwise direction, the distances from the inlet and the outlet to the center of the embankment are 5 m (= 75.8h = 25h_{emb}) and 7 m (= 106.1h = 35h_{emb}), respectively. In the cases of the simplified train model at the yaw angle of 50°, those are 5 m (= 75.8h = 25h_{emb}) and 10 m (= 151.5h = 50h_{emb}), respectively. The x coordinate axis corresponds to the streamwise direction; the y coordinate axis to the vertical direction; and the z coordinate axis to the spanwise direction. In addition, the two other axes are defined: the s axis along the embankment model and the n axis perpendicular to the embankment model. The origin of the coordinate axes coincides with the center of the embankment model at the floor level. In the cases of the train C model at yaw angles of 50° and 90°, and the simplified train model at the yaw angle of 90°, the center of the leading vehicle model is located in the middle of the computational domain (s = 0). In the cases of the simplified train model at the yaw angle of 50°, it is located at s = +1.6 m (= +8h_{emb}), +0.8 m (= +4h_{emb}), 0 m, and −1.6 m (= −8h_{emb}) (Fig. 9).

For the train C model, a velocity profile similar to that shown in Fig. 4 is imposed at the inlet, and it is constant in time. The velocity outside the boundary layer is 5 m/s. In the case of the simplified train model, the inlet condition is a block profile with a value of 5 m/s. The vertical profile of the streamwise velocity used as the inlet condition is shown in Fig. 10. In the case of the train C model, a velocity profile similar to that used in the experiments is used to replicate the wind tunnel tests in LES analyses. From a previous study (Suzuki et al., 2003), it is known that the side force coefficients of the train model on the embankment are affected by the boundary layer thickness even when the reference velocity U_{ref} is the same in the smooth flow cases. Thus, for the simplified train model, a block profile is used as the inlet condition to exclude the influence of the boundary layer thickness on the aerodynamic force coefficients. U_{ref} is 5 m/s, and a Reynolds number based on the car body height is approximately 0.2×10^5. The no-slip boundary condition is used on the surface of the leading vehicle model. Log-law-based wall functions are used on the surfaces of the dummy vehicles, the embankment, and the floor. However, for the simplified train model, a slip boundary condition is applied on the floor from the inlet to n = −0.45 m (= −2.25h_{emb}) to prevent boundary layer development. Slip boundary conditions are used on the side walls and the ceiling, as calculating the boundary layers on these walls have a large computational cost. At the outlet, all the velocity components are treated as gradient-free in the streamwise direction,

while the pressure is fixed.

The physical time step was 5×10^{-5} s ($t^* = tU_{ref}/h = 3.79 \times 10^{-3}$). This time step gives a maximum CFL number of about 2. The time-averaging was conducted for 1.3 s (t^* = 98.5) for the train C model and 1.5 s (t^* = 113.6) for the simplified train model, which was calculated after at least 2.3 s (t^* = 174) passed from the initial condition to obtain a fully developed turbulent flow.

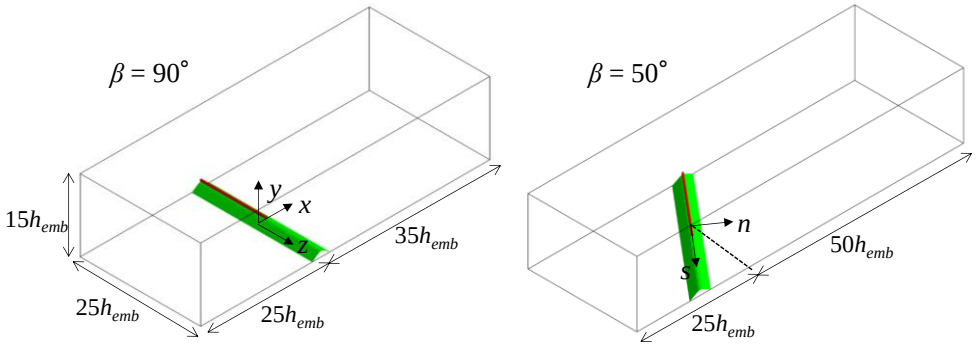

Fig. 8 Computational domains for the flow around the simplified train model

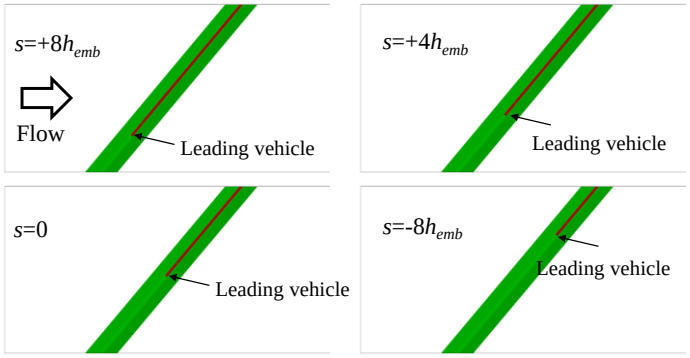

Fig. 9 Positions of the simplified train models at the yaw angle of 50°

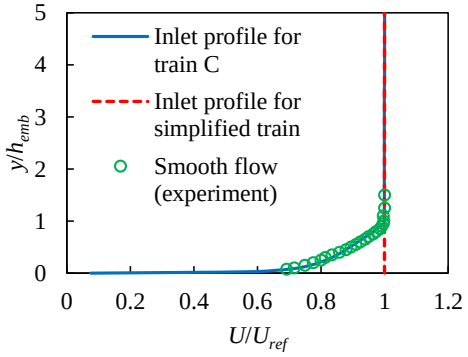

Fig. 10 Velocity profiles at the inlet

3.1.4 Computational grids

The surface mesh on the leading vehicle models is shown in Fig. 11. The spatial resolutions of the first cell layer on the leading vehicle models are listed in Table 2. Tetrahedral elements are used around the underfloor equipment of the complicated shape, while hexahedral elements are used elsewhere for the train C model. The maximum and the minimum grid spacing in the longitudinal direction of the leading vehicle are 2 mm (= $3.0 \times 10^{-2}h$) and 0.3 mm (= $4.6 \times 10^{-3}h$), respectively. The maximum and the minimum grid spacing in the circumferential direction of the leading vehicle are 2 mm (= $3.0 \times 10^{-2}h$) and 0.65 mm (= $9.9 \times 10^{-3}h$), respectively. The grids are concentrated near the upper corners of the vehicle in order to predict the flow separation precisely. The height of the first cells on the vehicle surface at the upper corners is 0.03 mm (= $4.6 \times 10^{-4}h$), and the grid stretching ratio ranges from 1.05 to 1.1. The spatial resolution expressed in the wall units (v/U_τ) was 0.4 in the wall-normal direction near the upper corner of the vehicle at the yaw angle of 90°. The total node numbers are approximately 30 million and 45 million for the yaw angles of 90° and 50° , respectively.

Hexahedral elements are used everywhere for the simplified train model. The maximum and the minimum grid spacing in the longitudinal direction of the leading vehicle are 3.3 mm (= $5.0 \times 10^{-2}h$) and 0.66 mm (= $1.0 \times 10^{-2}h$), respectively. The maximum and the minimum grid spacing in the circumferential direction of the leading vehicle are

1.9 mm (= $2.9 \times 10^{-2}h$) and 0.64 mm (= $9.7 \times 10^{-3}h$), respectively. The height of the first cells on the vehicle surface at the upper corners is 0.066 mm (= $1.0 \times 10^{-3}h$), and the grid stretching ratio is 1.13. The spatial resolution expressed in the wall units was approximately 1 in the direction normal to the wall near the upper corner of the vehicle at the yaw angle of 90°. At the yaw angle of 50°, the maximum grid spacing in the longitudinal direction on the embankment model is 25 mm (= $1.25 \times 10^{-1}h_{emb}$) ahead of the leading vehicle, and it is the same regardless of the position of the leading vehicle models. The total number of nodes is approximately 14 million for the yaw angle of 90°, and that ranges from 19 to 22 million for the yaw angle of 50°.

To investigate the influence of the grid resolution on the result, additional computations are made on the different grids of the simplified train model. The grid spacing in the longitudinal direction was varied while that in the circumferential and wall-normal direction was the same. For the yaw angle of 90°, the grid spacing of the coarse grid is three times as long as that of the fine grid, and that of the medium grid is 1.5 times as long as that of the fine grid. The grid spacing of the coarse grid is twice as long as that of the fine grid for the yaw angle of 50° where the leading vehicle is placed at $s = 0$. The total numbers of nodes used in the LES on the flow around the train model on the embankment are summarized in Table 3.

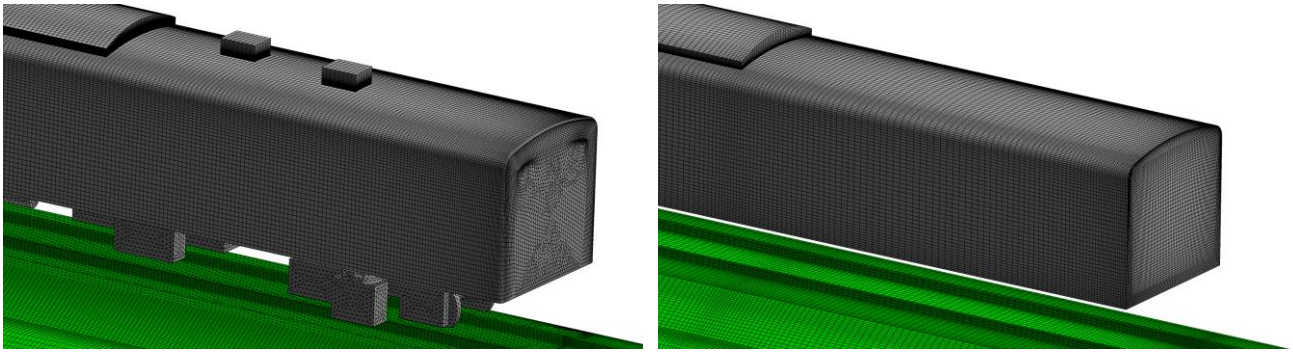

Fig. 11 Surface meshes of the fine grids

Table 2 Spatial resolutions of the first cell layer on the leading vehicle models

	Train C		Simplified train	
	Max	Min	Max	Min
Longitudinal direction	$3.0\times10^{-2}h$	$4.6\times10^{-3}h$	$5.0\times10^{-2}h$	$1.0\times10^{-2}h$
Circumferential direction	$3.0\times10^{-2}h$	$9.9\times10^{-3}h$	$2.9\times10^{-2}h$	$9.7\times10^{-3}h$
Wall-normal direction	-	$4.6\times10^{-4}h$	-	$1.0\times10^{-3}h$

Table 3 Total numbers of nodes in the grids

Yaw angle	Center of the vehicle	Train C	Simplified train		
		fine	coarse	medium	fine
90°	$s=0$	29.7M	4.9M	9.8M	14.2M
50°	$s=+8h_{emb}$	-	-	-	18.8M
	$s=+4h_{emb}$	-	-	-	19.5M
	$s=0$	44.9M	11.0M	-	20.1M
	$s=-8h_{emb}$	-	-	-	21.8M

3.2 Flow around an embankment model

LES on the flow around the train model on the embankment model shows that the longitudinal vortex emerging

near the upstream end of the embankment model distorts the flow field around the train model, which is described in section 4.2. In order to investigate the flow field around the embankment model in detail, LES analyses on the flow around the embankment model without train models were carried out at yaw angles of 90° and 50° for both block profile and ABL flows. The influence of the airflow condition on the flow around the embankment model was investigated. In addition, the influence of the spanwise width of the computational domain was examined at the yaw angle of 50°.

3.2.1 Model description

The embankment model used in LES analyses is the same as that shown in Fig. 2, and its characteristic length h_{emb} is 8/40 = 0.2 m. However, only the rail (height 0.004 m = 0.02h_{emb}) on the embankment is removed. The spanwise length of the computational domain is 5 m (=25h_{emb}) at the yaw angle of 90°, and is 2.5 m (=12.5h_{emb}), 5 m (=25h_{emb}) and 10 m (=50h_{emb}) at the yaw angle of 50°. The embankment models are extended from the side wall to the other one in all cases. In the ABL flow cases, the barrier, spires, and roughness blocks are located on the floor in the computational domain to replicate the wind tunnel tests.

3.2.2 Numerical method

In Section 3.2, numerical analyses on the flow around the embankment model were conducted using the commercial CFD code, ANSYS Fluent ver. 17.1, whereas Advance/ FrontFlow/ red ver. 5.2 was used in the analyses on the flow around the train models described in Section 3.1. The governing equations are the spatially filtered continuity and Navier–Stokes equations for an incompressible flow. The standard Smagorinsky model is used to model the sub-grid scale stresses. The value of the Smagorinsky coefficient is set as 0.1. The second-order central differencing scheme is applied for the convection term. The time integration is done using the second-order implicit scheme. The SIMPLE algorithm is used for the pressure–velocity coupling.

3.2.3 Computational domain and boundary condition

The size of the computational domains is summarized in Table 4. The computational domains with a spanwise length of 5 m at the yaw angle of 50° are shown in Fig. 12. As stated before, the *x* coordinate axis corresponds to the streamwise direction; the *y* coordinate axis to the vertical direction; and the *z* coordinate axis to the spanwise direction. In addition, two other axes are defined: the *s* axis along the embankment model and the *n* axis perpendicular to the embankment model. The origin of the coordinate axes coincides with the center of the embankment model with a spanwise length of 5 m at the floor level. The computational domain in the ABL flow cases has a height of 3 m (= 15h_{emb}) and a width of 5 m (= 25h_{emb}), and has dimensions similar to those of the test section of the experiments. In the streamwise direction, the distances from the inlet and the outlet to the center of the embankment are 17.84 m (= 89.2h_{emb}) and 7 m (= 35h_{emb}), respectively. For block-profile flow at the yaw angle of 90°, the computational domain has a height of 3 m (= 15h_{emb}) and a width of 5 m (= 25h_{emb}). The streamwise distances from the inlet and the outlet to the center of the embankment are 5 m (= 25h_{emb}) and 7 m (= 35h_{emb}), respectively. For block-profile flow at the yaw angle of 50°, the spanwise width of the computational domain is 2.5 m (= 12.5h_{emb}), 5 m (= 25h_{emb}), and 10 m (= 50h_{emb}). The streamwise length of the computational domain is adjusted as the length of the embankment model depends on the spanwise width of the computational domain. The height of the computational domain is 3 m (= 15h_{emb}).

The inlet condition is a block profile with a value of 5 m/s that is constant in time and space. In the block-profile

cases, a symmetry boundary condition is applied on the floor from the inlet to $n = -0.45$ m ($= -2.25h_{emb}$) to prevent the boundary layer development. No-slip boundary conditions are used on the surface of the embankment model and the floor except the region imposed on the slip boundary. In the ABL flow cases, no-slip boundary conditions are used on the surface of the embankment model, barrier, spires, roughness blocks, and the floor. Symmetry boundary conditions are used on the side walls and the ceiling. An outflow boundary condition is used at the outlet.

The physical time steps were 2×10^{-4} s ($t^* = tU_{ref}/h_{emb} = 5.0 \times 10^{-3}$) and 1×10^{-4} s ($t^* = 2.5 \times 10^{-3}$) for the block-profile cases and the ABL flow cases, respectively. These time steps give a maximum CFL number of about 1.5. The time-averaging was conducted from 5 s to 9 s ($t^* = 125$~225) and from 7 s to 19 s ($t^* = 175$~475) for the block-profile cases and the ABL flow cases, respectively.

The reference velocity U_{ref} is 5 m/s in the block-profile cases. In the ABL flow cases, U_{ref} is the velocity at $x = 0$ m, $y = 0.318$ m ($= 1.59h_{emb}$), and $z = 0$ m without the embankment model. This position corresponds to 4m height (full scale) above the rail level on the embankment. The Reynolds numbers based on h_{emb} and U_{ref} are approximately 0.7×10^5 in the block-profile cases and approximately 0.5×10^5 in the ABL flow cases.

Table 4 Summary of computational domains for flow around the embankment model

Yaw angle	Spanwise length	Block profile	ABL
90°	$25h_{emb}$	$-25 \le x/h_{emb} \le 35$ $0 \le y/h_{emb} \le 15$ $-12.5 \le z/h_{emb} \le 12.5$	$-89.2 \le x/h_{emb} \le 35$ $0 \le y/h_{emb} \le 15$ $-12.5 \le z/h_{emb} \le 12.5$
50°	$12.5h_{emb}$	$-25 \le x/h_{emb} \le 39.5$ $0 \le y/h_{emb} \le 15$ $0 \le z/h_{emb} \le 12.5$	-
	$25h_{emb}$	$-25 \le x/h_{emb} \le 50$ $0 \le y/h_{emb} \le 15$ $-12.5 \le z/h_{emb} \le 12.5$	$-89.2 \le x/h_{emb} \le 35$ $0 \le y/h_{emb} \le 15$ $-12.5 \le z/h_{emb} \le 12.5$
	$50h_{emb}$	$-25 \le x/h_{emb} \le 71$ $0 \le y/h_{emb} \le 15$ $-37.5 \le z/h_{emb} \le 12.5$	-

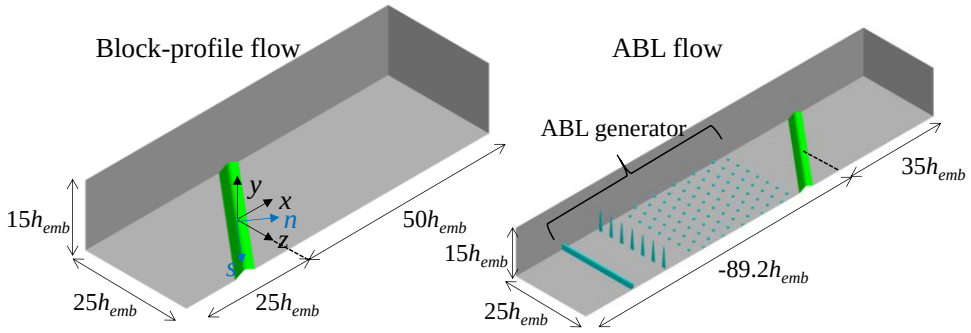

Fig. 12 Computational domains for the flow around the embankment model at the yaw angle of 50°

3.2.4 Computational grids

Hexahedral cells are used in the block-profile cases. At the yaw angle of 90°, the grid spacing in the spanwise direction is 25 mm ($= 1.25 \times 10^{-1}h_{emb}$). The maximum and the minimum grid spacing in the streamwise direction are 10 mm ($= 5.00 \times 10^{-2}h_{emb}$) and 1.9 mm ($= 9.50 \times 10^{-3}h_{emb}$), respectively. The height of the first cells on the surface of the no-slip walls is 0.05 mm ($= 2.50 \times 10^{-4}h_{emb}$), and the grid stretching ratio is 1.18. The spatial resolution of the

model expressed in the wall units (v/U_τ) was at most 2.5 and below 2 for almost all cells in the wall-normal direction at the yaw angle of 90°. The total numbers of cells included in the domains with the spanwise length of 5 m are approximately 6.4 (414 × 77 × 200) and 8.5 (439 × 77 × 250) million for yaw angles of 90° and 50°, respectively. That with the spanwise length of 10 m is approximately 18.3 (474 × 77 × 500) million, and that with the spanwise length of 2.5 m is approximately 4.2 (438 × 77 × 125) million. The spanwise grid spacing is constant even when the spanwise length of the computational domain is varied. In addition, different grids with spanwise lengths of 5 m are used to examine the grid dependency. The spanwise grid numbers in the coarse grid and the fine grid are one half and 1.5 times as many as those mentioned above, respectively; the grid numbers in the other directions are not changed.

In the ABL flow cases, the grids around the ABL generator, which are composed of hexahedral, tetrahedral, and prism cells, are connected to the hexahedral cells around the embankment model. The grids around the embankment model are the same as those used in the block-profile cases. The total number of cells around the ABL generator is approximately 4.2 million.

4. Results and discussion

4.1 Wind tunnel tests

First, the effects of the Reynolds number are described. C_S and C_L of the train models in ABL flow are shown in Fig. 13. The velocities measured by the pitot tube U_0 were 20 m/s, 25 m/s, and 30 m/s. Thus, Reynolds numbers based on U_{ref} (= $0.63U_0$) and the height of the car body were approximately 0.6×10^5, 0.8×10^5, and 0.9×10^5. C_L of train A and train B shows a little dependence on the Reynolds number as the roofs of train A and train B are rounder than those of the other train models. A separation point does not seem to be fixed on the roofs of train A and train B. However, a dependence on Reynolds number is hardly observed in C_S, which is the most important component for the train overturning. In this range of wind speeds, the effects of the Reynolds number on the aerodynamic force coefficients are not significant. As there is no significant sensitivity to the Reynolds number, only the results of U_0 = 30 m/s are reported below. In the smooth flow cases, this wind speed is equivalent to the Reynolds number of 1.5×10^5, which is almost the same value as that reported in Tomasini et al. (2014). Tomasini et al. (2014) have examined the sensitivity to the Reynolds number in the range of 4.4×10^4 to 2.2×10^5, and have compared the results at Re = 1.6×10^5.

C_S, C_L, and C_M in smooth and ABL flows are shown in Fig. 14 and Fig. 15. It is found that C_S is larger in ABL flow than in smooth flow at the yaw angle of 90° owing to the difference in the vertical profile of the mean wind speed between ABL flow and smooth flow. In smooth flow, C_S decreases as the yaw angle changes from 90° to 70°. However, C_S increases as the yaw angle changes from 70° to 50°, and C_S at the yaw angle of 50° is equal to or greater than that at the yaw angle of 90°. On the other hand, in ABL flow, C_S decreases as the yaw angle gets smaller, while the peak value cannot be detected. A similar trend can be seen with respect to the values of C_M. As for C_L, the peak values are observed at the yaw angle of 50° for both train C and train D in smooth flow and also in ABL flow, which is different from the C_S cases. For the other train models, the yaw angle at which C_L reaches its peak value cannot be observed clearly. It can be seen that the difference in the air flow characteristics has a distinct effect on C_S and C_M. In contrast, it has little effect on C_L. Therefore, the authors consider that factors other than the speed up effect on the slope of the embankment lead to this difference between smooth flow and ABL flow.

The aerodynamic force coefficients of the high-speed trains on the flat ground and the single track with ballast and rail (STBR) have been obtained (EN 14067-6, 2010), and it is well known that C_S achieves its maximum value at yaw angles between 40° and 60°. The aerodynamic force coefficients of the blunt-nosed German train (Silberling) on

the STBR ground configuration in smooth flow are shown in Fig. 14 (Paradot et al., 2015). C_S achieves its maximum value at the yaw angle of 60° and decreases monotonically as the yaw angle changes from 60° to 90°. A trend of C_S similar to Silberling has been observed for the other blunt-nosed trains on the flat ground although the peak of C_S is not as clear as that of the high-speed trains (Cheli et al., 2013; Giappino et al. 2016). However, C_S does not decrease monotonically as the yaw angle changes from 50° to 90° on the embankment configuration in smooth flow shown in Fig. 14.

The aerodynamic force coefficients in smooth flow have been compared with those in ABL flow on the viaduct and the flat ground (Bocciolone et al., 2008; Cheli et al., 2013; Kikuchi and Suzuki, 2015), and it is not notable that values of C_S are different between smooth flow and ABL flow. However, Fig. 14 and Fig. 15 indicate that C_S near the yaw angle of 50° is more affected by the airflow characteristics on the embankment configuration than that on the viaduct and the flat ground which was obtained in previous studies (Bocciolone et al., 2008; Cheli et al., 2013; Kikuchi and Suzuki, 2015).

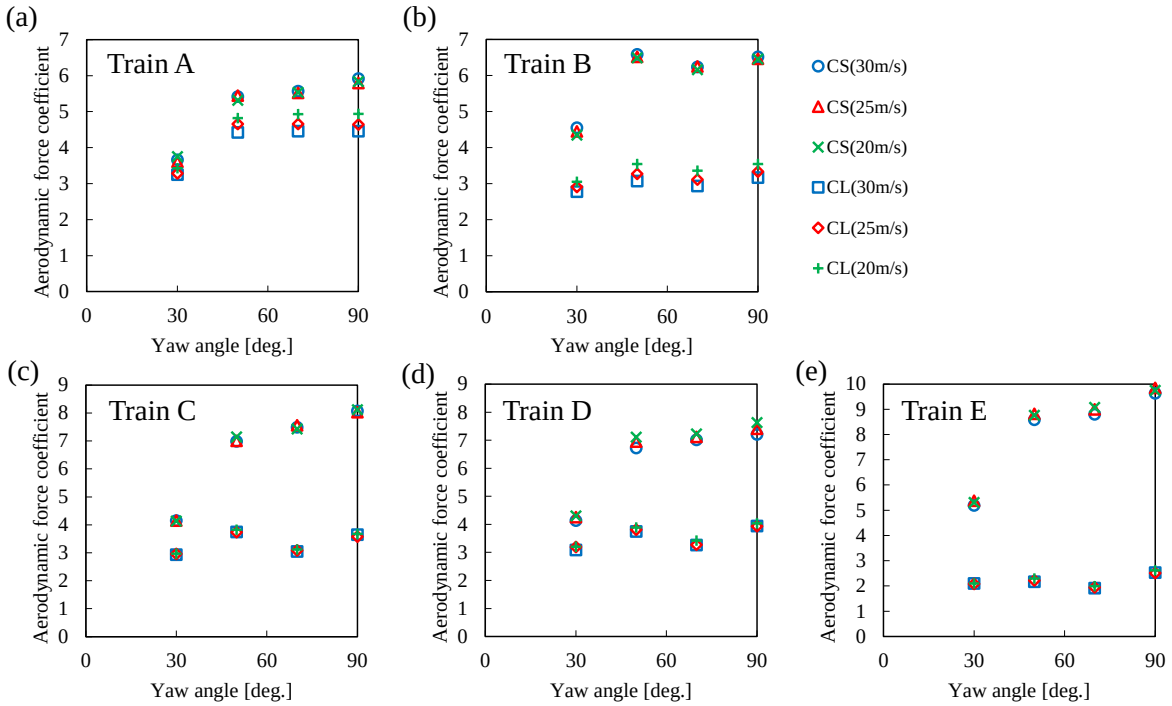

Fig. 13 Experimental values of C_S and C_L in ABL flow at different wind speeds

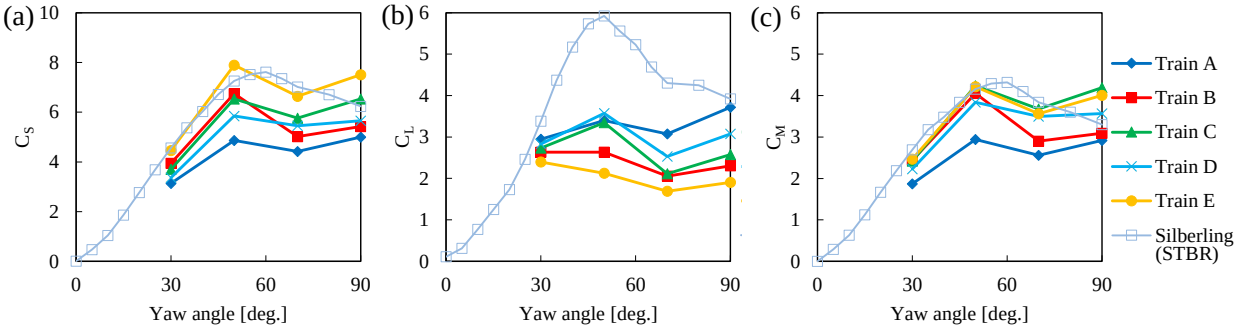

Fig. 14 Experimental values of C_S, C_L and C_M in smooth flow (U_0 = 30 m/s) (Paradot et al., 2015)

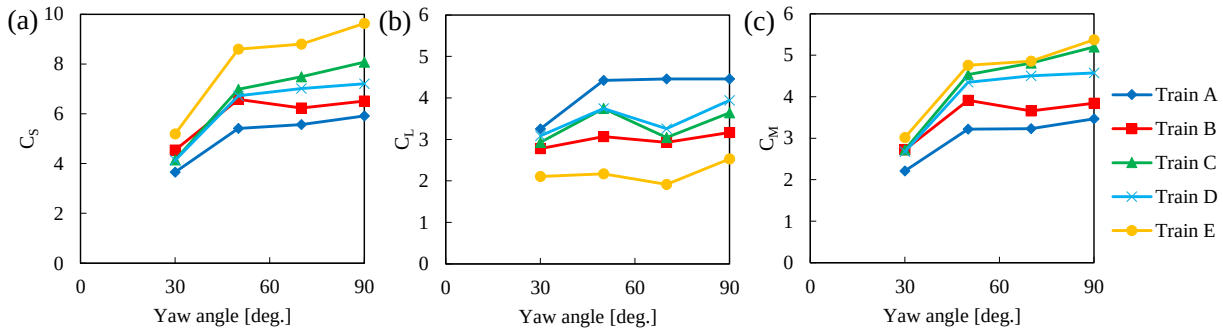

Fig. 15 Experimental values of C_S, C_L and C_M in ABL flow (U_0 = 30 m/s)

4.2 LES on the flow around train models on an embankment model

LES computations on the train C model in smooth flow were conducted at the yaw angles of 50° and 90° to replicate the wind tunnel tests. In addition, the distance between the simplified train model and the side wall was varied in LES computations, and the influence of the vehicle position on the aerodynamic force was investigated.

4.2.1 Grid dependency

First, the influence of the grid resolution on the results of the simplified train model is described. The grid spacing in the longitudinal direction was extended from the fine grid while that in the circumferential and wall-normal directions was not changed. Besides the fine grid, the coarse and medium grids were used, in which the grid spacing was three times and 1.5 times that of the fine grid at the yaw angle of 90°. At the yaw angle of 50°, the coarse grid was used, in which the grid spacing was twice that of the fine grid. The aerodynamic force coefficients of the coarse grid were almost the same as those of the fine grid at the yaw angle of 50°; thus, the medium grid was not used to perform the analysis at this yaw angle.

The time-averaged aerodynamic force coefficients of the simplified train models are shown in Table 5. The magnitude of C_L in the coarse grid at the yaw angle of 90° has a positive value, and a negative value in the medium and fine grids at the yaw angle of 90°. Although there is a difference in the coarse grid at the yaw angle of 90°, the influence of the grid resolution can be hardly noted in the other cases. The good agreement between the fine grids and the other grids indicates that the resolution of the fine grids is sufficient to predict the time-averaged flow field at this Reynolds number. Hemida and Krajnović (2010) conducted an LES study on the high-speed train model at yaw angles of 90° and 35° at Reynolds numbers of 3.0×10^5 and 3.7×10^5, and confirmed that the distribution of the time-averaged surface pressure obtained by LES was in good agreement with the experimental data. The node numbers in the grids used by Hemida and Krajnović (2010) are 11.5 million and 14 million at yaw angles of 90° and 35°. In the LES study described in this report, the node numbers in the fine grids are 14.2 million and 20.1 million at yaw angles of 90° and 50° although the Reynolds number is small ($Re = 0.2 \times 10^5$). The number of nodes required to resolve the boundary layer with LES is in proportion to $Re^{1.8}$ (Piomelli and Balaras, 2002). Therefore, the authors consider that the grid resolution is sufficient to predict the time-averaged flow field for this Reynolds number. In the next section, LES results regarding the train C model are described. In LES analyses on the train C model, grids finer than those used for the simplified train model are applied to resolve the flow around the bogies and the underfloor equipment. The numbers of nodes in the grids for the train C model are 29.7 million and 44.9 million at yaw angles of 90° and 50°.

Table 5 Time-averaged aerodynamic force coefficients of the simplified train model in LES computations

Yaw angle	Grid	C_S	C_L	C_M
90°	Coarse	8.17	0.57	5.49
	Medium	8.54	-0.58	5.63
	Fine	8.45	-0.59	5.57
50°	Coarse	6.55	4.05	4.49
	Fine	6.39	4.17	4.36

4.2.2 Flow field around the train model

In this section, LES results of the train C model in smooth flow are described. Table 6 reports the time-averaged aerodynamic force coefficients obtained from the simulations and the experiments. The obtained LES values of C_S and C_M are reasonably in good agreement with those obtained in the experiments, whereas the C_L value obtained by LES deviates from the experimental value. This is probably because the turbulence intensity near the floor of the wind tunnel was not reproduced in LES, in addition to the presence of a difference in Reynolds numbers between LES and the experiments. It is pointed out that the lift force is affected by the local roughness in close proximity to the train model (Baker et al., 2004). In this LES, only the mean velocity profile was given at the inlet boundary, and the turbulence was not reproduced. This lack of flow turbulence led to the difference in the flow under the train model, which probably caused the discrepancy in C_L. However, C_S and C_M are in good agreement with the experimental values, and contribute to approximately 90% of the rolling moment about the leeward rail and, in this case, are more important for vehicle overturns than C_L. Thus, the LES results correctly reproduced the effect of the change in the yaw angle.

The isosurfaces of the instantaneous and time-averaged pressure coefficient at the yaw angle of 90° are shown in Fig. 16, and those at the yaw angle of 50° are shown in Fig. 17. The reported values of both the instantaneous and time-averaged pressure coefficients are −0.9. This coefficient is defined by the time-averaged static pressure divided by $0.5\,\rho\,U_{ref}^2$. At the yaw angle of 90°, the flow around the train is almost two-dimensional except in the vicinity of the front of the leading vehicle. In contrast, the flow around the train is highly three-dimensional at the yaw angle of 50°. In this case, a strong vortex is generated near the upstream end of the embankment model adjacent to the sidewall, and a strong negative pressure spreads to the center of the computational domain. In instantaneous flow, the negative pressure generated near the upstream end of the embankment merges with that generated by the train model on the leeward side of the train. The flow around the train model on the embankment model seems to be affected not only by the flow near the train but also by the vortex generated near the end of the embankment model at the yaw angle of 50°.

Table 6 Time-averaged aerodynamic force coefficients of the train C model

Yaw angle	Experiment			LES		
	C_S	C_L	C_M	C_S	C_L	C_M
90°	6.54	2.57	4.19	6.85	2.05	4.49
50°	6.54	3.35	4.24	7.08	2.22	4.65

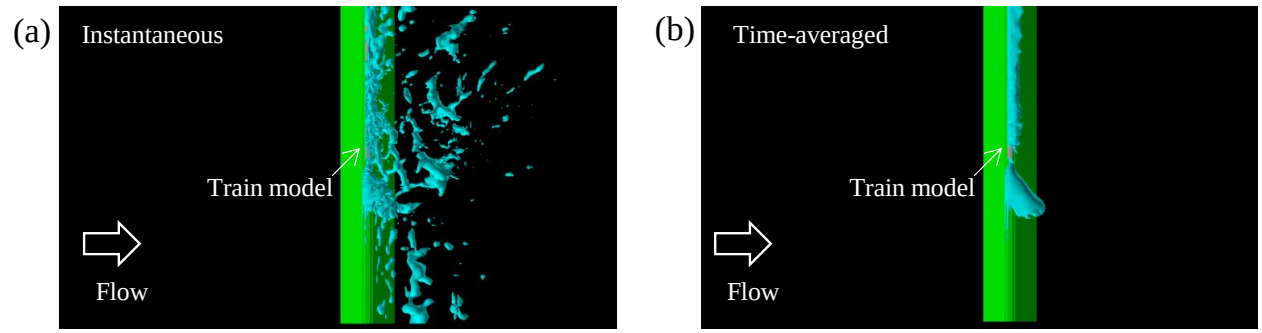

Fig. 16 Isosurface of the instantaneous and time-averaged pressure coefficients ($C_p = -0.9$) at the yaw angle of 90°

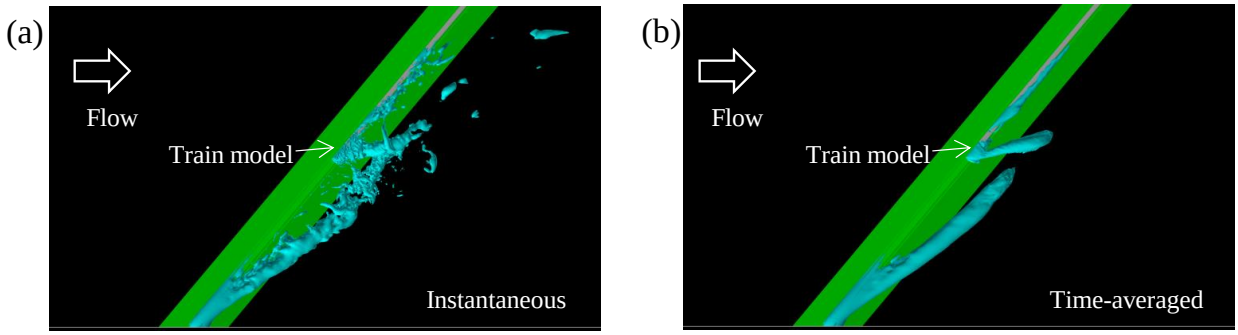

Fig. 17 Isosurface of the instantaneous and time-averaged pressure coefficients ($C_p = -0.9$) at the yaw angle of 50°

4.2.3 Effect of the position of the vehicles

The previous section suggests that the negative pressure emerging from the upstream end of the embankment model affects the flow around the train model at the yaw angle of 50°. In this section, LES computations were conducted to investigate the influence of the distance from the simplified train model to the side wall on the aerodynamic forces at the yaw angle of 50°. The center of the car body of the train model was located at $s = +8h_{emb}$, $+4h_{emb}$, 0, and $-8h_{emb}$ at the yaw angle of 50° (Fig. 9).

Table 7 reports the time-averaged aerodynamic force coefficients obtained by LES computations. C_S of the simplified train model at the yaw angle of 90° is larger than that of the train C model shown in Table 6 though the simplified train model does not have any underfloor equipment. This is attributed to the difference in the boundary layer thickness of the inlet flow (fig. 10). Table 7 clearly shows that C_S at the yaw angle of 50° highly depends on the position of the vehicle or the distance from the upstream end of the embankment model. When the train model is near the upstream end of the embankment model, C_S at the yaw angle of 50° is larger than that at the yaw angle of 90°. C_S at the 50° yaw angle becomes smaller as the distance from the train model to the upstream end of the embankment becomes larger. Figure 18 shows the distribution of the time-averaged pressure coefficient on the x-y plane at the center of the leading vehicle at the yaw angle of 50°. Figure 18 (a) shows the case of the train model at $s = +8h_{emb}$ (closest to the upstream end of the embankment), and Fig. 18 (b) shows the case of the train model at $s = -8h_{emb}$ (farthest from the upstream end of the embankment). In the case of $s = +8h_{emb}$, the strong negative pressure occurs in the leeward of the embankment model, which leads to a stronger negative pressure on the leeward side of the train model at $s = +8h_{emb}$ than that of the train model at $s = -8h_{emb}$. As a result, C_S becomes large in the case of the train model at $s = +8h_{emb}$. The LES study on the simplified train model shows that the vortex generated near the upstream end of the embankment model has a significant influence on not only the flow around the train model, but also the side force coefficient.

Table 7 Time-averaged aerodynamic force coefficients of the simplified train model

Yaw angle	Vehicle postion	LES		
		C_S	C_L	C_M
90°	s =0	8.45	-0.59	5.57
50°	s =+8h_{emb}	9.24	1.59	6.23
	s =+4h_{emb}	7.55	2.55	5.09
	s =0	6.39	4.17	4.36
	s =-8h_{emb}	6.21	4.27	4.25

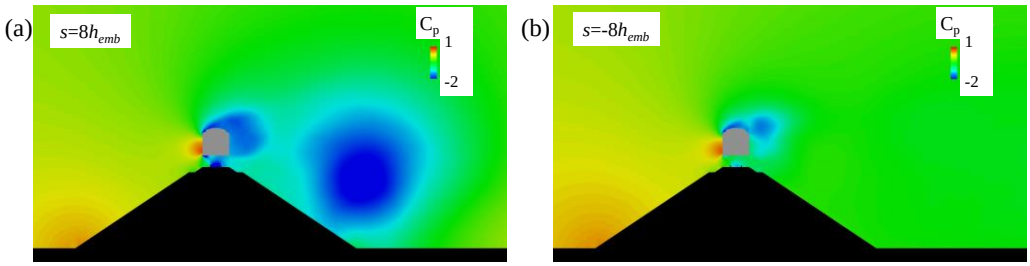

Fig. 18 Time-averaged pressure coefficient on the *x*-*y* plane at the center of the leading vehicle at the yaw angle of 50°: (a) train model at $s = 8h_{emb}$ and (b) train model at $s = -8h_{emb}$

4.3 LES on the flow around an embankment model

LES computations on the flow around the embankment model without train models were conducted at yaw angles of 90° and 50°. The spanwise length of the computational domain was varied to investigate its influence on the flow around the embankment model with a block-profile flow. In addition, ABL flow was simulated in LES, and the effects of the airflow characteristics on the flow field around the embankment model were investigated.

4.3.1 Grid dependency

To investigate the influence of the grid resolution, LES computations were conducted using different grids with a spanwise length of 5 m. The inlet condition is a block profile without ABL generators. The numbers of cells in the grids are 414 × 77 × 100 (coarse), 414 × 77 × 200 (medium), and 414 × 77 × 300 (fine) at the yaw angle of 90°. Those at the yaw angle of 50° are 439 × 77 × 125 (coarse), 439 × 77 × 250 (medium), and 439 × 77 × 375 (fine). At the yaw angle of 90°, the grid spacing of each grid in the spanwise direction is 0.25h_{emb}, 0.125h_{emb}, and 0.083h_{emb}.

Figure 19 shows the spanwise profiles of the time-averaged pressure coefficient (static pressure) above the embankment model at (x, y) = (0, 1.385h_{emb}) and (x, y) = (1.32h_{emb} (=4h), 1.385h_{emb}) at the yaw angle of 90°. The position at (x, y) = (0, 1.385h_{emb}) coincides with that of the center of the car body discussed in the previous section. There is little difference in the profiles at x = 0. However, the profile of the coarse grid slightly deviates from that of the medium and fine grids at x = 4h. Figure 20 shows the s-direction profiles of the time-averaged pressure coefficient above the embankment model at (n, y) = (0, 1.385h_{emb}) and (n, y) = (1.32h_{emb} (=4h), 1.385h_{emb}) at the yaw angle of 50°. A good agreement between the medium and fine grids is obtained at the yaw angle of 50°. Although the resolution of the coarse grids is poor, the influence of the grid resolution on the time-averaged pressure around the embankment model is not significant. As the results obtained by the medium grids and the fine grids are almost the same, the results obtained by the medium girds are reported below. In the ABL flow cases, longer simulation time is needed to obtain the time-averaged flow field than in the smooth flow cases; therefore, fine grids were not used to avoid high computational cost.

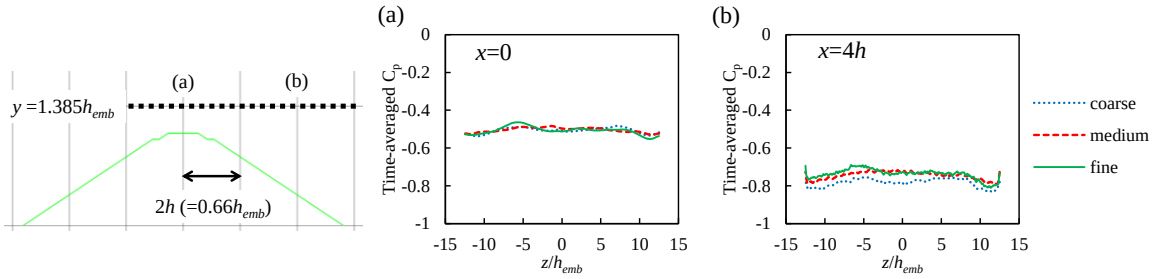

Fig. 19 Spanwise profiles of the time-averaged pressure coefficient above the embankment model at $y = 1.385h_{emb}$ for the yaw angle of 90°: (a) $x = 0$ and (b) $x = 1.32h_{emb}$ (= $4h$)

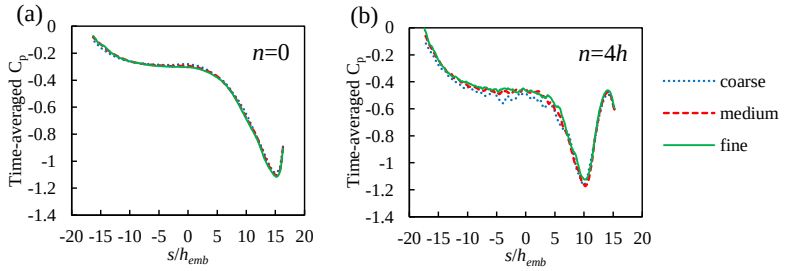

Fig. 20 s-direction profiles of the time-averaged pressure coefficient above the embankment model at $y = 1.385h_{emb}$ for the yaw angle of 50°: (a) $n = 0$ and (b) $n = 1.32h_{emb}$ (= $4h$)

4.3.2 Flow field around the embankment model

In this section, the inlet condition is a block profile without ABL generators. As shown in Fig. 21, time-averaged velocities in the n-direction and s-direction are referred to as U' and W' in addition to U, V, and W, which are time-averaged x-velocity, y-velocity, and z-velocity, respectively. It has been known that Prandtl's independence principle holds for incompressible laminar flow over a yawed airfoil whose spanwise length is infinite (Schlichting, 1979). According to this principle, the flow on the n-y plane is independent of that in the s-direction. Thus, the flow on the n-y plane remains unchanged when the configuration is yawed. In turbulent flow, the Reynolds stress couples the flow on the n-y plane with that in the s-direction, and this principle no longer strictly holds. However, it is experimentally shown that this principle approximately holds over a certain range of yaw angles for flow behind a swept backward-facing step (Selby, 1983 and Fernholz et al., 1993). Baker (1985) investigated the acceleration of the natural wind over an embankment with wind tunnel tests and on-site measurements, and demonstrated that only the velocity perpendicular to the embankment is accelerated while that parallel to the embankment remains unchanged at yaw angles between 90° and 30°. It implicitly means that Prandtl's independence principle can be applied to flow over the swept embankment.

Figure 22 shows the s-direction profiles of time-averaged velocities (U', V and W') at $(n, y) = (0, 1.385h_{emb})$ for the cases with the yaw angle of 50° and spanwise lengths of $12.5h_{emb}$, $25h_{emb}$, and $50h_{emb}$. For comparison, U and V averaged in the spanwise direction ($-5 \leq z/h_{emb} \leq 5$) for the yaw angle of 90° at the same points are shown. At the yaw angle of 50°, U' and V are normalized by $U_{ref}\sin(50°)$, and W' is normalized by $U_{ref}\cos(50°)$. At the yaw angle of 90°, U and V are normalized by U_{ref}. U' and V at the yaw angle of 50° significantly differ from U and V at the yaw angle of 90° near the upstream end of the embankment ($s > 10h_{emb}$). They get closer to the values of the yaw angle of 90° away from the upstream end of the embankment, and they match the values of the yaw angle of 90° at $s < 0$ except in the proximity of the downstream end of the embankment, which means that the independence principle partly holds for flow above the embankment model. As for W', the value of $W'/U_{ref}\cos(50°)$ at $n = 0$ remains -1 except in the proximity

of the side wall (Fig. 22 (c)). In the case with the spanwise length of 12.5h_{emb}, the velocities at the yaw angle of 50° do not match those at the yaw angle of 90° as the width of the computational domain is too small compared with the embankment height. When the spanwise length is too small compared with the embankment height, flow over the embankment model is distorted by the longitudinal vortex generated near the upstream end of the embankment model.

Figure 23 shows the *s*-direction profiles of the time-averaged pressure coefficient at (*n*, *y*) = (0, 1.385h_{emb}) and (*n*, *y*) = (1.32h_{emb} (=4*h*), 1.385h_{emb}) for the cases with the yaw angle of 50° and spanwise lengths of 12.5h_{emb}, 25h_{emb} and 50h_{emb}. For comparison, time-averaged pressure coefficients averaged in the spanwise direction ($-5 \leq z/h_{emb} \leq 5$) for the yaw angle of 90° at the same points are shown. It is noted that the pressure coefficient is defined by the static pressure normalized by $0.5\rho\{U_{ref}\sin(50°)\}^2$ for the yaw angle of 50°, while it is defined by that normalized by $0.5\rho U_{ref}^2$ for the yaw angle of 90°. As is the case with the velocity, the coefficient at the yaw angle of 50° does not match that at the yaw angle of 90° in the case with the spanwise length of 12.5h_{emb}. Figure 24 shows the *s*-direction profiles of the time-averaged pressure coefficient in the case with the yaw angle of 50° and the spanwise length of 25h_{emb} at (*n*, *y*) = (0, 1.385h_{emb}) (Fig. 23 (a)) and the relation between C_S and the position of the train model (Table 7). It is clearly shown that the relation between C_S and the position of the train model traces a similar trend to the longitudinal profile of the pressure coefficients above the embankment model.

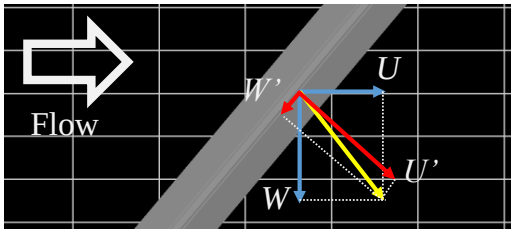

Fig. 21 Definition of *U'* and *W'* for cases with the yaw angle of 50°

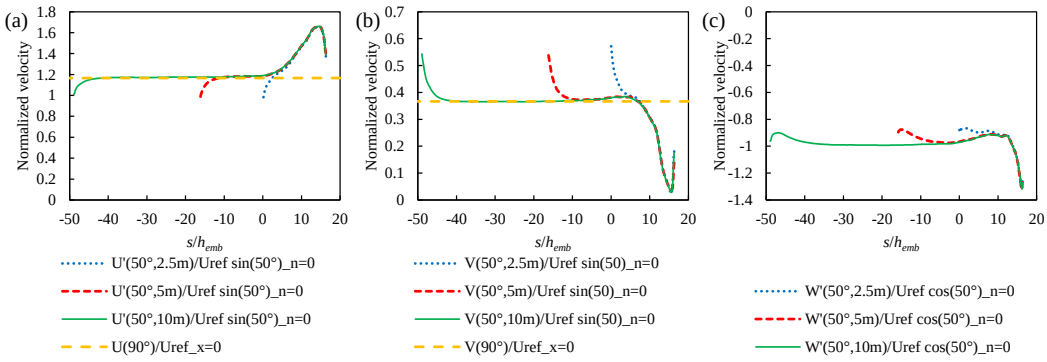

Fig. 22 *s*-direction profiles of time-averaged velocities at (*n*, *y*) = (0, 1.385h_{emb}): (a) *U'*, (b) *V* and (c) *W'*

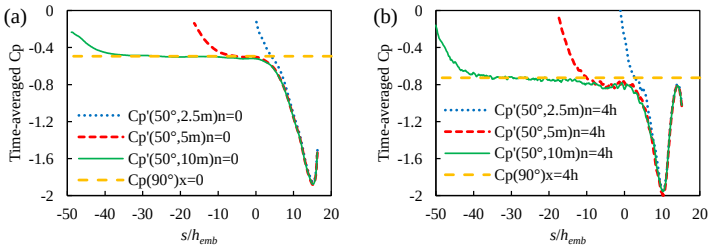

Fig. 23 *s*-direction profiles of time-averaged pressure coefficient: (a) (*n*, *y*) = (0, 1.385h_{emb}) and (b) (*n*, *y*) = (1.32h_{emb} (= 4*h*), 1.385h_{emb})

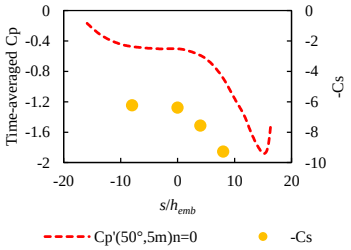

Fig. 24 *s*-direction profiles of time-averaged pressure coefficient at (n, y) = (0, 1.385h_{emb}) and the relation between C_S and the position of the train model for the case with a yaw angle of 50° and a spanwise length of 25h_{emb}

4.3.3 Effect of the airflow characteristics

In this section, the influence of the airflow condition on the flow around the embankment model is described. The ABL flow shown in Fig. 4 is replicated in LES computations. The width of the computational domain is 5 m (= 25h_{emb}). Figure 25 shows the vertical profiles of the time-averaged x-velocity and the turbulence intensity in the x-direction, y-direction, and z-direction at (x, z) = (0, 0) in the ABL flow without the embankment model. The results obtained in LES are in good agreement with the experiment, and LES computations reproduce the airflow used in the experiment well. Figure 26 shows the comparison of the vertical profiles of U and V obtained by LES with experimental values for the yaw angle of 90° at (n, z) = (−3h_{emb}/8, 0) and (n, z) = (3h_{emb}/8, 0). Figure 27 shows these values for the yaw angle of 50° at the same positions. In the experiments, the velocity was measured by a hot-wire anemometer with an X wire probe (Saitou et al, 2008). The velocity is normalized by U_{ref}. U obtained by LES is a little smaller than that in the experiments at n = −3h_{emb}/8 (windward side) near the surface of the embankment model for both yaw angles. However, U and V agree reasonably well with the experimental values at n = −3h_{emb}/8, and the airflow going up along the slope is well reproduced in LES computations. U and V agree well with the experimental values at n = 3h_{emb}/8 (leeward side) for both yaw angles, and the flow separation on the top of the embankment model is well captured in LES computations.

Figure 28 shows the comparison of the vertical profiles of U', V, and W' between the ABL flow and block-profile flow at (x, z) = (0, 0). As was the case with the previous section, U' and V are normalized by U_{ref} sin(50°), and W' is normalized by U_{ref} cos(50°) for the yaw angle of 50°. For the yaw angle of 90°, the velocity (only U and V) is normalized by U_{ref}. In the both flows, the profiles of U' at yaw angles of 50° and 90° are in agreement, as are the profiles of V, which means that the independence principle approximately holds for the flow above the embankment model even during ABL flow. This results are verified by Baker (1985). As for W' at the yaw angle of 50°, W'/U_{ref} cos(50°) is −1 except near the surface of the embankment model in the block-profile flow while it is less than −1 in the ABL flow at y = 1.385h_{emb} which corresponds to the height of the center of the car body.

Figure. 29 shows a comparison of the s-direction profiles of the time-averaged pressure coefficients between ABL flow and block-profile flow at (n, y) = (0, 1.385h_{emb}) and (n, y) = (1.32h_{emb} (=4h), 1.385h_{emb}). For comparison, time-averaged pressure coefficients averaged in the spanwise direction ($-5 \leq z/h_{emb} \leq 5$) for the yaw angle of 90° at the same points are shown. The pressure coefficient is defined by the static pressure normalized by $0.5\rho\{U_{ref}\sin(50°)\}^2$ for the yaw angle of 50° while it is defined by that normalized by $0.5\rho U_{ref}^2$ for the yaw angle of 90°. In both flows, a large negative pressure occurs near the upstream end of the embankment model at the yaw angle of 50°. The minimum value of the coefficients in block-profile flow is lower than that in ABL flow at the yaw angle of 50°, though the span-averaged value in block-profile flow is higher than that in ABL flow at the yaw angle of 90°. It suggests that the vortex

emerging near the upstream end of the embankment model is stronger in block-profile flow than in ABL flow. For both $s/h_{emb} \leq 4$ in ABL flow and $s/h_{emb} \leq 0$ in block-profile flow, the coefficient at the yaw angle of 50° is almost the same as that at the yaw angle of 90° at $n = 0$ (Fig.29 (a)). The distance from the upstream end of the embankment model, which is necessary for the pressure recovery, is shorter in ABL flow than in block-profile flow. At $n = 4h$, the coefficient at 50° yaw angle takes the same value as that at 90° yaw angle for $s/h_{emb} \leq 2$ in the ABL flow (Fig.29 (b)). However, in block-profile flow, the coefficient at the yaw angle of 50° is a little lower than that at the yaw angle of 90° even in $-5 \leq s/h_{emb} \leq 0$ owing to the large negative pressure near the upstream end of the embankment model. The range where the independence law approximately holds is wider in ABL flow than in block-profile flow.

Figure 30 shows the comparison of the distribution of the time-averaged y-velocity V on the x-z plane at $y = h_{emb}$ between ABL flow and block-profile flow at the yaw angle of 50°; Fig. 31 shows these values corresponding to the instantaneous y-velocity on the same plane. The time-averaged and instantaneous y-velocities are normalized by U_{ref} in Fig. 30 and Fig. 31. In the time-averaged flow field (Fig. 30), a strong flow in the downward direction occurs near the upstream end of the embankment model on the leeward side in both airflows, and the flow passing over the embankment is dragged into the separated region. In block-profile flow, a strong flow in the upward direction between the embankment model and the downward flow is observed, which implies generation of the strong longitudinal vortex. In contrast, the upward flow between the embankment model and the downward flow cannot be observed clearly in ABL flow. In the instantaneous flow field (Fig. 31), the upward flow on the leeward side is clearly observed in block-profile flow. However, it does not clearly appear owing to the disturbance of the large-scale turbulence in ABL flow. In summary, the influence of the longitudinal vortex extends away from the upstream end of the embankment model; however, the range where its influence exists is smaller in ABL flow than in block-profile flow owing to large-scale turbulence.

When the aerodynamic forces are measured using the static train model on the embankment model, the longitudinal vortex emerges near the side wall and modifies the flow field around the embankment model even with the wall-to-wall extension of the embankment model. In LES analyses described above, the distance necessary to mitigate the influence of this vortex is $16h_{emb}$ from the upstream end of the embankment model in block-profile flow and $12h_{emb}$ in ABL flow at the yaw angle of 50°.

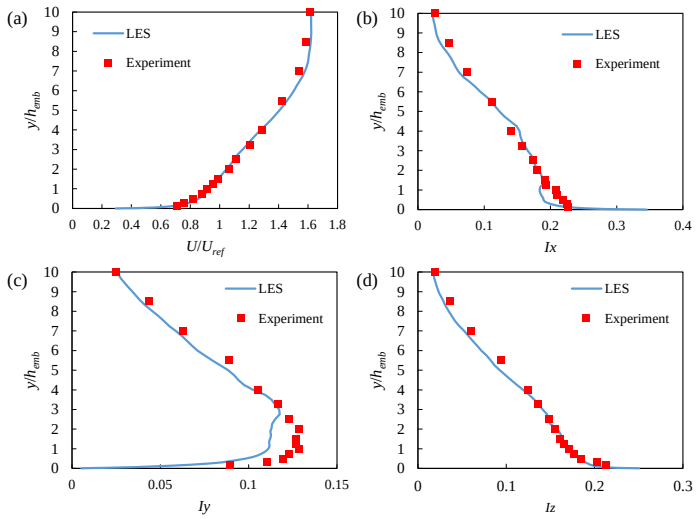

Fig. 25 Comparison of the vertical profiles of the ABL flow without the embankment model at (x, z) = (0, 0): (a) time-averaged x-velocity and turbulence intensity in the (b) x-direction, (c) y-direction, and (d) z-direction

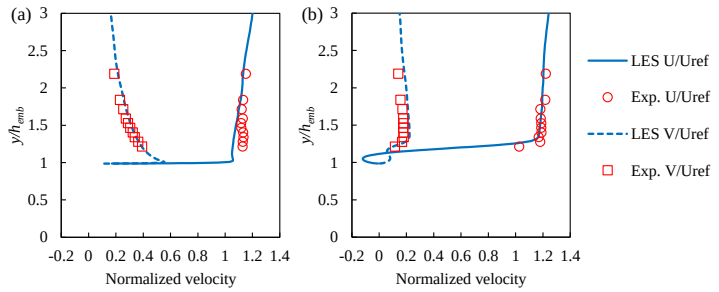

Fig. 26 Comparison of the vertical profiles of U and V at the yaw angle of 90°: (a) (n, z) = ($-3h_{emb}/8$, 0) and (b) (n, z) = ($3h_{emb}/8$, 0)

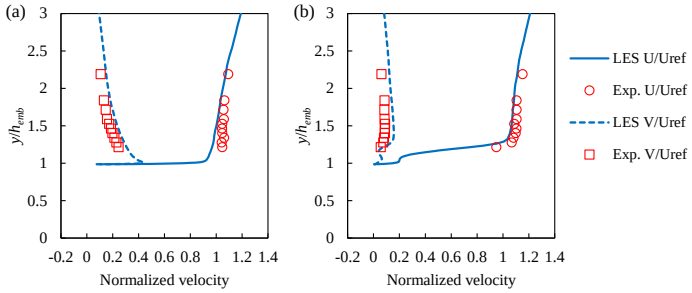

Fig. 27 Comparison of the vertical profiles of U and V at the yaw angle of 50°: (a) (n, z) = ($-3h_{emb}/8$, 0) and (b) (n, z) = ($3h_{emb}/8$, 0)

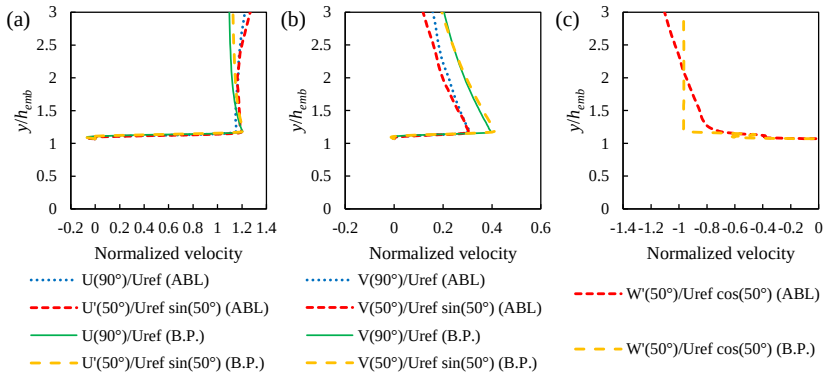

Fig. 28 Vertical profiles of the velocity in the different airflow conditions at (x, z) = (0, 0): (a) U', (b) V, and (c) W'

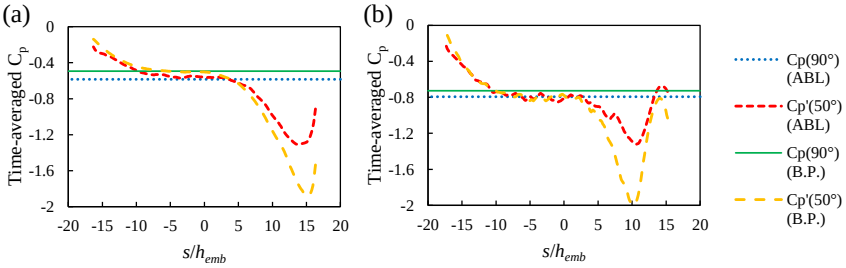

Fig. 29 s-direction profiles of the time-averaged pressure coefficients in the different airflow conditions: (a) (n, y) = (0, $1.385h_{emb}$) and (b) (n, y) = ($1.32h_{emb}$ (=$4h$), $1.385h_{emb}$)

(a) (b)

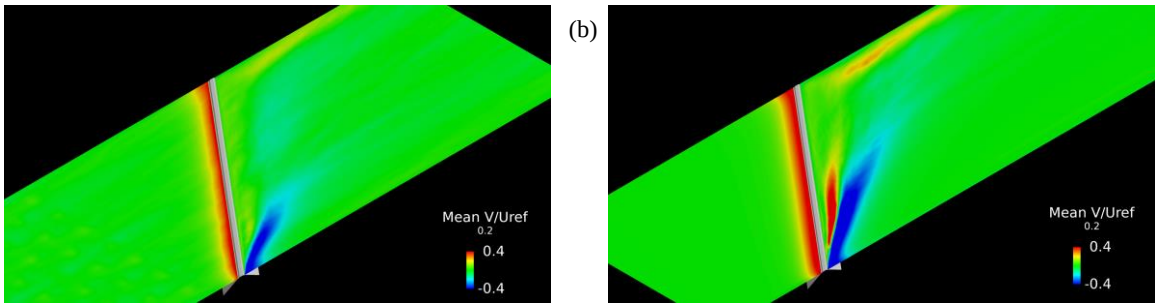

Fig. 30 Distribution of the time-averaged y-velocity at $y = h_{emb}$ for the yaw angle of 50°: (a) ABL flow and (b) block-profile flow

(a) (b)

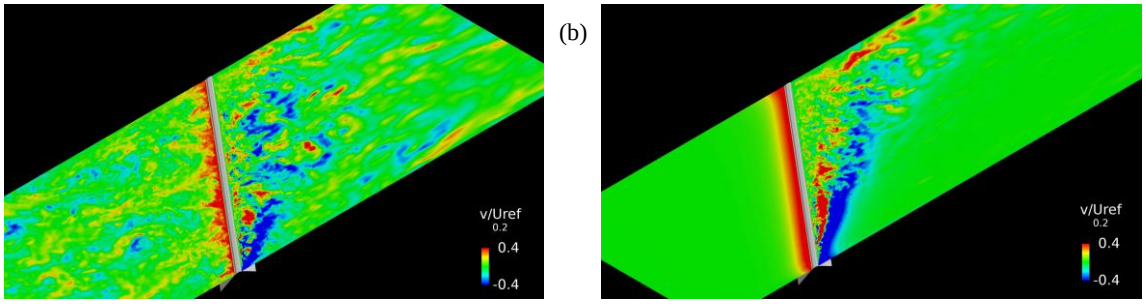

Fig. 31 Distribution of the instantaneous y-velocity at $y = h_{emb}$ for the yaw angle of 50°: (a) ABL flow and (b) block-profile flow

5. Conclusions

Wind tunnel tests were carried out to determine the aerodynamic force coefficients of train models on the embankment model in both the ABL and smooth flows with the embankment model extended to the side walls. LES analyses on the flow around the train model on the embankment model were conducted during the smooth flow at yaw angles of 90° and 50°, and the influence of the proximity to the side wall was investigated. LES analyses on the flow around the embankment model were also conducted to examine the effect of the airflow conditions.

In smooth flow, the side force coefficients at the yaw angle of 50° are greater than those at the 70° yaw angle, and are equal to or greater than those at the yaw angle of 90°. On the other hand, the side force coefficients at the yaw angle of 50° are smaller than those at the yaw angle of 70°, and such a peak of the side force coefficient cannot be observed in ABL flow.

LES analyses show that the flow around the train model is almost two-dimensional except in the vicinity of the front of the vehicle at the yaw angle of 90°. However, at the yaw angle of 50°, a longitudinal vortex emerges near the upstream end of the embankment model and extends to the middle of the computational domain, which affects the flow on the leeward side of the train model. The side force coefficient increases as the distance from the train model to the upstream end of the embankment model gets shorter at the yaw angle of 50°. The relation between the side force coefficient and the position of the train model traces a similar trend to the longitudinal profile of the time-averaged static pressure above the embankment model.

LES analyses on the flow around the embankment model without train models show that Prandtl's independence principle does not hold for the flow above the embankment model near its upstream end owing to the longitudinal vortex at the yaw angle of 50°. However, the independence principle partly holds at the yaw angle of 50° away from the end of the embankment model in both the ABL and block-profile flows. The distance necessary for the

independence principle to hold is $16h_{emb}$ from the upstream end of the embankment model in block-profile flow and $12h_{emb}$ in ABL flow at the yaw angle of 50°.

When the influence of the relative movement between the train model and the embankment model is investigated in the experiment, the aerodynamic forces acting on the static train model need to be measured. From this study, an embankment model long enough to satisfy these values must be used when comparing the aerodynamic forces obtained through static model tests with those obtained through moving model tests. Meanwhile, the Reynolds number in this LES study is lower than that in the wind tunnel tests. The influence of the Reynolds number on the longitudinal vortex should be examined in the future.

Acknowledgements

This research was conducted as a part of the Joint Research initiated in 2016 by Railway Technical Research Institute, Japan and the University of Birmingham, UK.

Funding

This research did not receive any specific grant from funding agencies in the public, commercial, or not-for-profit sectors.

References

- Baker, C.J., 1985. The determination of topographical exposure factors for railway embankments. J. Wind Eng. Ind. Aerodyn. 21, 89-99.
- Baker, C.J., 1986. Train aerodynamic forces and moments from moving model experiments. J. Wind Eng. Ind. Aerodyn. 24, 227-251.
- Baker, C.J., 1991. Ground vehicles in high cross winds part I: Steady aerodynamic forces. J. Fluids Struct. 5, 69-90.
- Baker, C.J., Jones. J., Lopez-Calleja, F., Munday, J., 2004. Measurements of the cross wind forces on trains. J. Wind Eng. Ind. Aerodyn. 92, 547-563.
- Baker, C., Cheli, F., Orellano, A., Paradot, N., Proppe, C., Rocchi, D., 2009. Cross-wind effects on road and rail vehicles. Veh. Syst. Dyn. 47 (8), 983-1022.
- Baker, C., 2010. The flow around high speed trains. J. Wind Eng. Ind. Aerodyn. 98, 277-298.
- Baker, C., 2013. A framework for the consideration of the effects of crosswinds on trains. J. Wind Eng. Ind. Aerodyn. 123, 130-142.
- Bocciolone, M., Cheli, F., Corradi, R., Muggiasca, S., Tomasini, G., 2008. Crosswind action on rail vehicles: Wind tunnel experimental analyses. J. Wind Eng. Ind. Aerodyn. 96, 584-610.
- Cheli, F., Corradi, R., Rocchi, D., Tomasini, G., Maestrini, E., 2010. Wind tunnel tests on train scale models to investigate the effect of infrastructure scenario. J. Wind Eng. Ind. Aerodyn. 98, 353-362.
- Cheli, F., Giappino, S., Rosa, L., Tomasini, G., Villani, M., 2013. Experimental study on the aerodynamic forces on railway vehicles in presence of turbulence. J. Wind Eng. Ind. Aerodyn. 123, 311-316.
- Diedrichs, B., Sima, M., Orellano, A., Tengstrand, H., 2007. Crosswind stability of a high-speed train on a high embankment. Proc. Inst. Mech. Eng. Part F J. Rail Rapid Transit 221, 205-225.

- Dorigatti, F., Sterling, M., Baker, C.J., Quinn, A.D., 2015. Crosswind effects on the stability of a model passenger train–A comparison of static and moving experiments. J. Wind Eng. Ind. Aerodyn. 138, 36-51.
- EN 14067-6, 2010. Railway Applications – Aerodynamics – Part 6: Requirements and Test Procedures for Cross Wind Assessment. CEN, Brussels.
- Fernholz, H.-H., Janke, G., Kalter, M., Schober, M., 1993. On the separated flow behind a swept backward-facing step. In: Gersten, K. (Ed.), Notes on Numerical Fluid Mechanics, 40. Vieweg, pp. 200-207.
- García, J., Muñoz-Paniagua, J., Jiménez, A., Migoya, E., Crespo, A., 2015. Numerical study of the influence of synthetic turbulent inflow conditions on the aerodynamics of a train. J. Fluids Struct. 56, 134-151.
- Giappino, S., Rocchi, D., Schito, P., Tomasini, G., 2016. Cross wind and rollover risk on lightweight railway vehicles. J. Wind Eng. Ind. Aerodyn. 153, 106-112.
- Hemida, H., Krajnović, S., 2010. LES study of the influence of the nose shape and yaw angles on flow structures around trains. J. Wind Eng. Ind. Aerodyn. 98, 34-46.
- Khier, W., Breuer, M., Durst, F., 2000. Flow structure around trains under side wind conditions: a numerical study. Computers & Fluids 29, 179-195.
- Kikuchi, K., Suzuki, M., 2015. Study of aerodynamic coefficients used to estimate critical wind speed for vehicle overturning. J. Wind Eng. Ind. Aerodyn. 147, 1-17.
- Krajnović, S., Ringqvist, P., Nakade, K., Basara, B., 2012. Large eddy simulation of the flow around a simplified train moving through a crosswind flow. J. Wind Eng. Ind. Aerodyn. 110, 86-99.
- Nakade, K., 2014. Numerical simulation of flow around railway vehicle in turbulent boundary layer over flat terrain. Q. Rep. RTRI 55 (4), 249-254.
- Paradot, N., Grégoire, R., Stiepel, M., Blanco, A., Sima, M., Deeg, P., Schroeder-Bodenstein, K., Johnson, T., Zanetti, G., 2015. Crosswind sensitivity assessment of a representative Europe-wide range of conventional vehicles. Proc. Inst. Mech. Eng. Part F J. Rail Rapid Transit 229, 594-624.
- Piomelli, U., Balaras, E., 2002. Wall-layer models for large-eddy simulations. Annu. Rev. Fluid Mech. 34, 349-374.
- Premoli, A., Rocchi, D., Schito, P., Tomasini, G., 2016. Comparison between steady and moving railway vehicles subjected to crosswind by CFD analysis. J. Wind Eng. Ind. Aerodyn. 156, 29-40.
- Robinson, C.G., Baker, C.J., 1990. The effect of atmospheric turbulence on trains. J. Wind Eng. Ind. Aerodyn. 34, 251-272.
- Saitou, H., Ido, A., Tanemoto, K., Suzuki, M., 2008. Characteristics of wind velocity distribution over embankment in turbulent boundary layer obtained by wind tunnel experiment. RTRI Rep. 22 (5), 51-56 (in Japanese).
- Sanquer, S., Barré, C., Dufresne de Virel, M., Cléon, L.M., 2004. Effect of cross winds on high-speed trains: development of a new experimental methodology. J. Wind Eng. Ind. Aerodyn. 92, 535-545.
- Schlichting, H., 1979. Boundary-Layer Theory. McGraw-Hill, pp. 247-254.
- Schober, M., Weise, M., Orellano, A., Deeg, P., Wetzel, W., 2010. Wind tunnel investigation of an ICE 3 endcar on three standard ground scenarios. J. Wind Eng. Ind. Aerodyn. 98, 345-352.
- Selby, G.V., 1983. Applicability of the independence principle to subsonic turbulent flow over a swept rearward-facing step. AIAA J. 21 (11), 1603-1604.
- Suzuki, M., Tanemoto, K., Maeda, T., 2003. Aerodynamic characteristics of train/vehicles under cross winds. J.

Wind Eng. Ind. Aerod. 91, 209-218.

- Suzuki, M., Tanemoto, K., Noguchi, Y., 2014. Field test and wind tunnel test on aerodynamic force coefficients of train/vehicles in cross winds. In: Proceedings of the 11th UK Conference on Wind Engineering, pp. 155-158.
- Suzuki, M., 2016. Method of wind tunnel test on aerodynamic characteristics of vehicle under cross wind by using moving model rig. RTRI Rep. 30 (7), 41-46 (in Japanese).
- Suzuki, M., Hibino, Y., 2016. Field tests and wind tunnel tests on aerodynamic characteristics of train/vehicles under crosswinds. Q. Rep. RTRI 57 (1), 55-60.
- Tomasini, G., Giappino, S., Corradi, R., 2014. Experimental investigation of the effects of embankment scenario on railway vehicle aerodynamic coefficients. J. Wind Eng. Ind. Aerodyn. 131, 59-71.
- Tsubokura, M., Kobayashi, T., Nakashima, T., Nouzawa, T., Nakamura, T., Zhang, H., Onishi, K., Oshima, N., 2009. Computational visualization of unsteady flow around vehicles using high performance computing. Computers & Fluids 38, 981-990.